ADVANCED MATERIALS
www.advmat.de

Capillary-Driven 3D Open Fluidic Networks for Versatile Continuous Flow Manipulation

Shuangmei Wu, Siqi Sun, Jia Ye, Liqiu Wang, and Yiyuan Zhang**

Human civilization hinges on the capability to manipulate continuous flows. However, continuous flows are often regulated in closed-pipe configurations to address their instability, isolating the flows from the environment and considerably restricting their functionality. Manipulating continuous flows in open systems remains challenging. Here, capillary-driven 3D open fluidic networks (OFNs) composed of connected polyhedral frames are reported. Each frame acts as a fluid chamber with free interfaces that enable fluid entry and exit; the connecting rods function as valves, allowing precise control over the direction, velocity, and path of the flow. The OFNs seamlessly adapt to various fluid systems, enabling precise 3D manipulation of multiple flows. Leveraging these distinctive features, a series of applications, including selective metallization, programmable mixing and diagnostics, and spatiotemporal control of multi-step reactions, are achieved. The OFNs' free fluid interfaces also facilitate controlled drug release and efficient heat exchange. These versatile OFNs will significantly advance technological innovations in engineering, microfluidics, interfacial chemistry, and biomedicine.

1. Introduction

Fluids serve as essential carriers of mass, momentum, energy, information, and life. The precise manipulation of 3D continuous flows holds transformative potential for advancing multidisciplinary applications ranging from microfluidic organ-on-a-chip systems[1,2] to precision medical diagnostics,[3,4] next-generation chemical synthesis,[5,6] smart material fabrication,[7] and energy system optimization.[8,9] Current fluidic technologies often confine continuous flows within closed pipe systems due to the inherent fluidity and instability of fluids.[10,11] Conventional closed pipe systems, reliant on external pumps and different types of valves equipped in the pipes, control the direction, speed, and path of the flows, however, the rigid walls of the pipes also significantly hinder 3D spatial fluidic interactions with the operational environment.[12–14] This confinement limits the fluid's ability to enter and exit freely, engage in chemical reactions, and transfer mass, energy and information, substantially curtailing the versatility needed for diverse applications.[15–17] It remains a great challenge to design a multifunctional fluidic platform capable of precise and programmable 3D spatiotemporal control over multiple continuous flows.[18–20]

Here, we address this challenge with the capillary-driven 3D open fluidic networks (OFNs) composed of interconnected polyhedral frame units, where each frame unit functions as a chamber for the storage and transport of fluids, while the free interface maintained by each frame serves as gateways for fluid entry and exit, and the connecting rods between the frames function as valves, enabling control over the direction, speed, and path of the continuous flow. Notably, the fluid undergoes moving on and between 3D scaffold networks and can spontaneously form a continuous capillary flow within the OFNs, driven by capillary forces, without the need for external energy. The architectures of OFNs can be directly fabricated through 3D printing technology, allowing for precise tuning of unit-cell structures, spatial configurations, and feature sizes to regulate capillary action and enable programmability. The direction, speed, and path of multiple continuous flows can be flexibly programmed in 3D space by varying the number and arrangement of connecting rods, as well as the geometric parameters and shapes of the frames. Furthermore, by adjusting the surface wettability and geometric parameters of the OFNs, this system can be adapted for the manipulation of continuous flows of diverse fluids in different environments, including water in air, air in water, water in oil, and oil in water. In addition to effectively handling immiscible fluids, OFNs can also be employed in miscible fluid systems through interfacial gelation, such as facilitating the manipulation of continuous flows of aqueous solutions in water. Thus, OFNs represent a versatile fluidic tool capable of programmably and precisely controlling unary, binary, and multiple continuous flows in both spatial and temporal dimensions. This is exemplified through selective metallization, programmable spatiotemporal control of binary fluid mixing

S. Wu, S. Sun, J. Ye, L. Wang, Y. Zhang
Department of Mechanical Engineering
The Hong Kong Polytechnic University
Hong Kong 999077, China
E-mail: liqiu.wang@polyu.edu.hk; yi-yuan.zhang@polyu.edu.hk

The ORCID identification number(s) for the author(s) of this article can be found under https://doi.org/10.1002/adma.202503840

DOI: 10.1002/adma.202503840

processes, dual-model ion detection, and multi-step chemical reactions, as well as applications aimed at enhancing interfacial mass transfer and heat transfer. To highlight the applicability, practical utility, and key advantages of OFNs, we provide a summary of the limitations of existing fluidic techniques, the unique features of OFNs, and six applications that illustrate the advantages of OFNs over traditional fluidic technologies in Table S11 (Supporting Information).

2. Results and Discussion

2.1. Capillary-Driven 3D Open Fluidic Networks

The OFNs are composed of 3D polyhedral frames and connecting rods, with each frame unit functioning as a fluid chamber capable of storing and carrying fluid; the free interfaces of each frame serve as gateways for fluid entry and exit, facilitating the introduction or extraction of target fluid from any frame in the network; the connecting rods work as fluid valves, allowing for precise regulation of the direction, velocity, and flow path of the continuous flow (**Figure** 1A). Precise, programmable, and versatile manipulation of continuous flow is readily realized by tuning the critical parameters of the frame unit (surface wettability, geometry, side length, and rod diameter) and the connecting rods (quantity, diameter, and spatial arrangement), to meet various application needs. For instance, horizontal directional transport is accomplished by setting a single-rod connection as a stop valve within the network (Figure 1B,C; Movie S1, Supporting Information). Continuous flows in the direction of gravity, as well as against it, are facilitated by altering the fluid inlet position (Figure 1D,E; Movie S1, Supporting Information). Increasing the number of connecting rods effectively enhances the flow speed of spontaneous capillary flow within the network (Figure 1F; Movie S2, Supporting Information); the experimental results indicate that when the number of connecting rods is increased from 2 to 4 and 6, the flow rate increases by 56% and 177%, respectively (Figure 1G), with these enhancements attributed to greater capillary forces. Variations in the double-rod arrangement orientation and length result in subtle effects on flow velocity through adjusted hydrodynamic resistance (Figure S10 and S11, Supporting Information). Using asymmetric and symmetric distributions of connecting rods within the network leads to asymmetric and symmetric capillary force distributions, thus enabling the differential and equal flow velocities on either side of the network, respectively (Figure 1H; Movie S3, Supporting Information). Alterations to the geometry of the frames can also generate a capillarity gradient, facilitating precise spatiotemporal control over the flow path of the fluid within the network (Figure 1I; Movie S3, Supporting Information). Consequently, with a predesigned OFN, it is easy to achieve programmable spatiotemporal control of continuous flows in 3D space (Movie S4, Supporting Information), allowing 2D patterning of one fluid (Figure S12, Supporting Information) as well as 3D patterning of multiple fluids (Figure 1J).

2.2. Working Mechanisms and Design Principles of the OFNs

For horizontal flow with negligible effects of gravity, the basic prerequisite for using OFNs to manipulate continuous flow is that the target fluid can form spontaneous capillary flow in OFNs driven by the capillarity (**Figure** 2A,B). Physically, the formation of spontaneous capillary flow in OFN requires that the solid surface has a stronger affinity for fluid 1 than for fluid 2, that is,

$$\theta_{123} < \frac{\pi}{2} \tag{1}$$

where θ_{123} is the contact angle of fluid 1 on solid 3 in fluid 2 (Figure 2C).

Geometrically, the polyhedral frame units in OFNs need to provide free interfaces to allow the entry and exit of fluids, thus requiring

$$r < X \tag{2}$$

where r is the rod radius of polyhedral frame units, X is the radius of the inscribed circle of the faces of polyhedral frame units (Figure 2D,E).

Dynamically, the fluid replacement process (Figure 2B) must be dominated by the capillarity. Therefore, the characteristic length of the created fluid interfaces (L) should be within the capillary length (L_c), namely

$$L < L_c \tag{3}$$

L and L_c can be determined by $L = 2C_1(a - 2 * \frac{r}{\tan\frac{\phi}{2}})$ and $L_c = \sqrt{\frac{\gamma_{12}}{\Delta\rho g}}$. a is the side length of polyhedral frame units; C_1 is a constant determined by the geometry of the frames which is defined by $X = C_1\, a$; ϕ is the interior angle of the faces of polyhedral frame units; γ_{12} and $\Delta\rho$ are the interfacial tension and density difference between fluid 1 and fluid 2, respectively; and g is the acceleration of gravity. The specific values of C_1 and ϕ for polyhedral frames of various geometries are included in Text S1 (Supporting Information).

From the perspective of energy, it must be satisfied that the total energy of the system after fluid replacement E_2 is less than the initial total energy of the system E_1,

$$E_2 < E_1 \tag{4}$$

which indicates that fluid 1 can spontaneously form a continuous capillary flow in OFNs without external energy input. Substituting the specific energy expression into Equation (4) and combining it with Young's equation, yields

$$\frac{A_{12}}{A_{13}} < \cos\theta_{123} \tag{5}$$

where A_{12}, A_{13} are the interfacial areas between fluid 1 and fluid 2 and contact areas between fluid 1 and solid 3 (Figure 2D), respectively. The detailed derivation of Equation (5) is included in Text S2 (Supporting Information). Therefore, to successfully manipulate continuous flows in any fluid system, the design principles of OFNs need to satisfy the abovementioned physical, geometric, and dynamic conditions. The mathematical expression of the boundary conditions for the formation of spontaneous

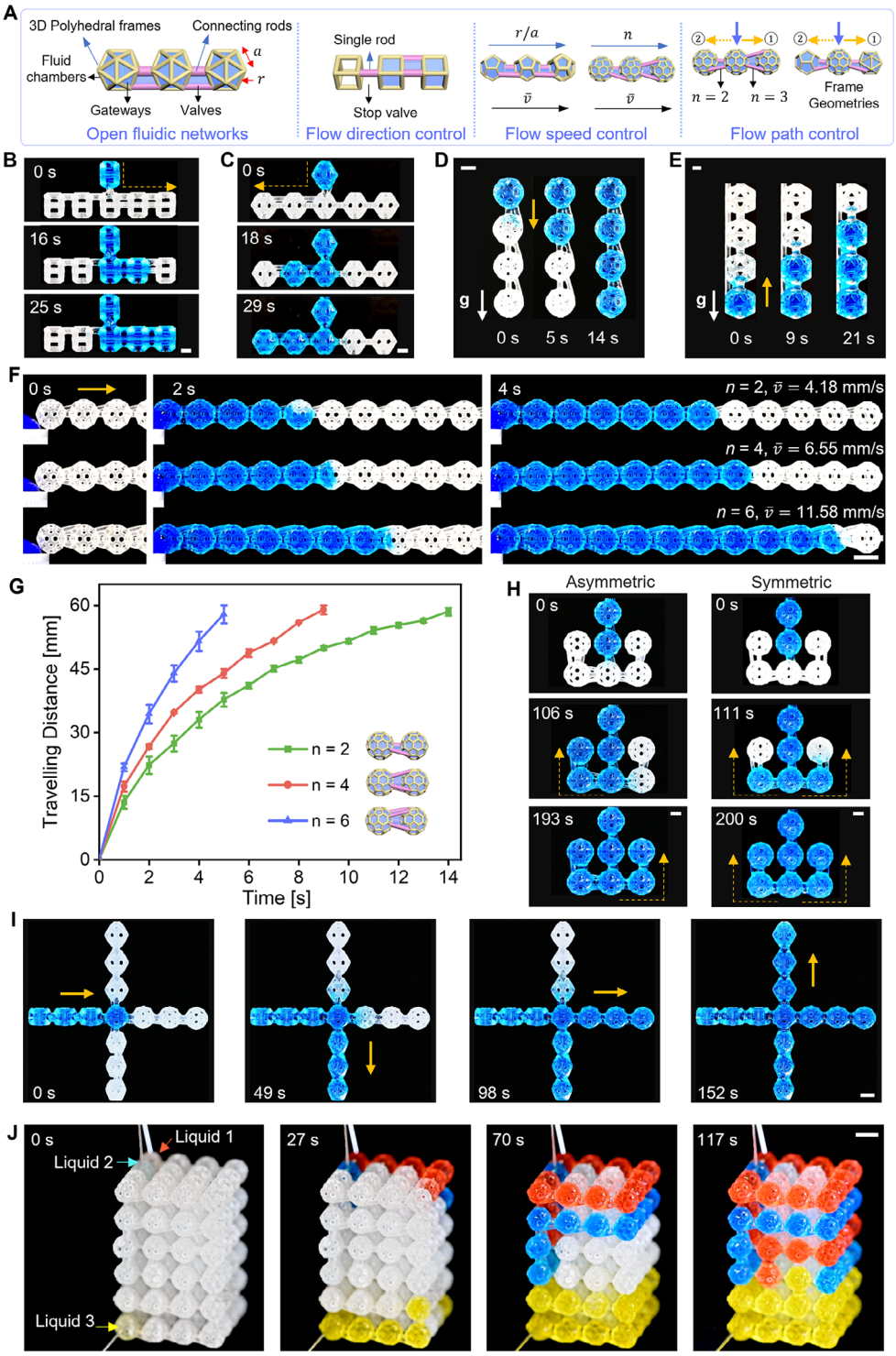

Figure 1. Precise, programmable, and versatile manipulation of continuous flow with the OFNs. A) Schematic diagram of the OFNs. The direction, speed, and path of the continuous flow in the network can be precisely controlled by adjusting the key parameters of polyhedral frames and connecting rods. *a* and *r* are the side length and rod radius of the frame units, respectively. *n* refers to the number of the connecting rod and $\bar{v}$ is the velocity of the continuous flow. B–E) Control of the flow direction, including horizontal directional flows (B and C), and directional flows along (D) and against (E) the gravity. Scale bar, 1 mm. F), G) Control of the flow speed. (F) The speed of the spontaneous capillary flow in the OFNs increases with the number of connecting rods (*n*). Scale bar, 4 mm. (G) Curve of the travelling distance of the front of spontaneous capillary flow in the OFNs versus time. H,I) Control of the flow path. The flow path of the fluid is controlled by changing the arrangement of connecting rods (H) and the geometry of the frames in the network (I). J) Programmable spatiotemporal control of multiple continuous flows in 3D space. In H–J, the scale bars are 2 mm. In B–F and H–J, fluids have been dyed by different dyes to facilitate visualization. The details are provided in the Experimental Section.

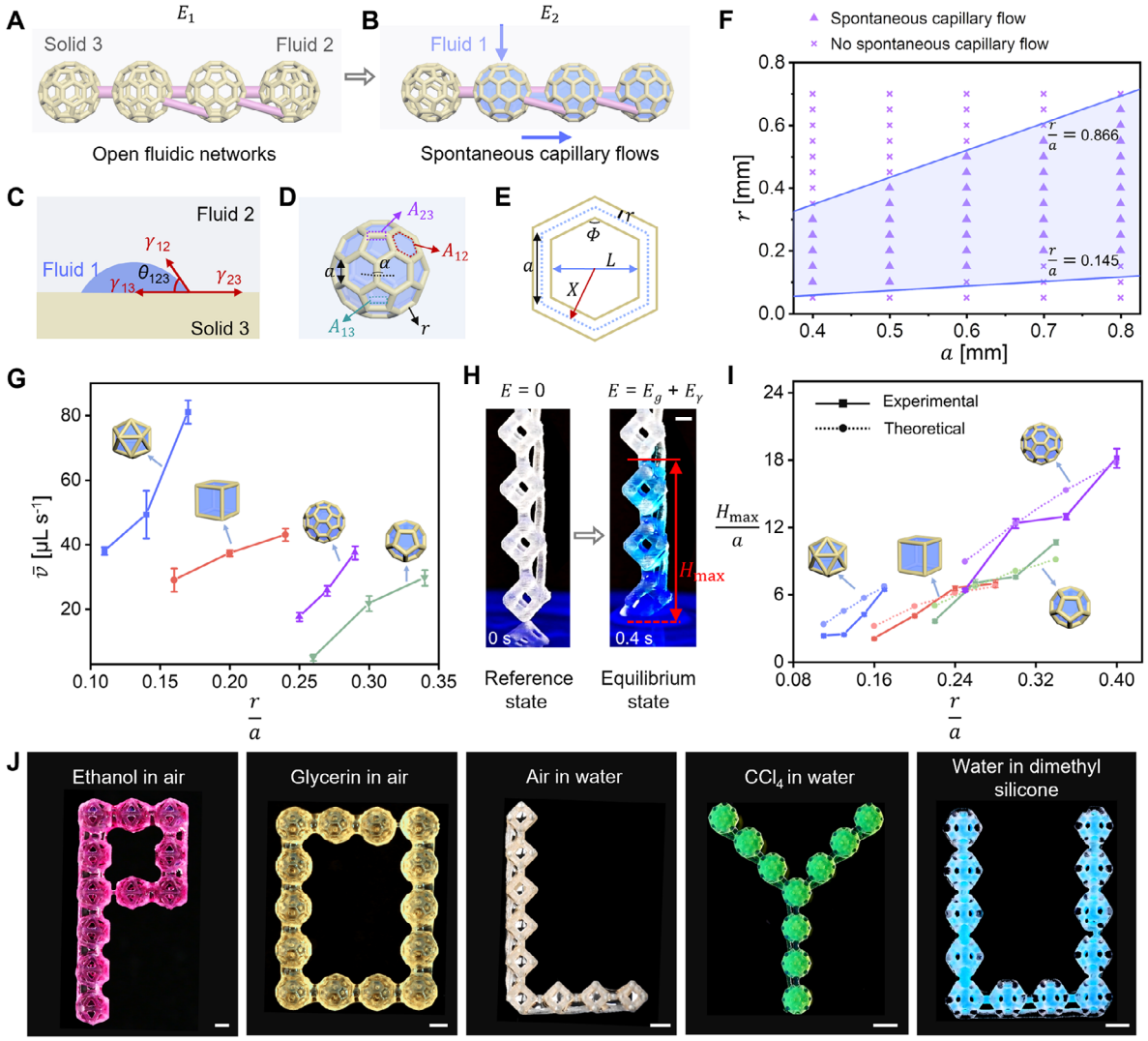

Figure 2. Working mechanisms and design principles of the OFNs. A,B) The process that fluid 1 replaces fluid 2 to form spontaneous capillary flows in the OFNs (solid 3). C–E) The key geometric parameters of the OFNs. γ_{12}, γ_{13}, and γ_{23} are the interfacial tension of fluid 1–fluid 2, fluid 1–solid 3, and fluid 2–solid 3, respectively. A_{12}, A_{13}, and A_{23} are the interfacial area of fluid 1–fluid 2, fluid 1–solid 3, and fluid 2–solid 3, respectively. F) Effect of geometry parameters of the OFNs on spontaneous capillary flow creation of water in air. r is the frame rod radius. a is the frame side length. The upper and lower blue lines are $r/a = 0.866$ and $r/a = 0.145$, respectively. The triangle and cross icons indicate successful creation and no spontaneous capillary flow, respectively. The highlighted purple region includes the safe geometry parameters for spontaneous capillary flow formation. G) Dependence of average flow rate $\bar{v}$ on the $\frac{r}{a}$ of OFNs of different geometries. H) Capillary rise in the OFNs. The initial state before liquid rising is used as the reference state. H_{max} is the maximum capillary rise height. Scale bar, 1 mm. I) Experimentally measured and theoretically calculated $\frac{H_{max}}{a}$ of OFNs with different geometry and size parameter $\frac{r}{a}$. J) The wide applicability of OFNs to different fluidic systems. Scale bar, 2 mm. In H, J, fluids have been dyed by different dyes to facilitate visualization. The details are provided in the Experimental Section.

capillary flow in OFNs can be summarized as the following set of equations,

$$\begin{cases} \theta_{123} < \frac{\pi}{2} \\ a - \frac{2r}{\tan\frac{\theta}{2}} < \frac{1}{2C_1}\sqrt{\frac{\gamma_{12}}{\Delta\rho g}} \\ \frac{C_1 C_2}{C_2 \sin\theta_{123} + (\pi - 2\theta_{123} + \alpha) C_1 n \cos\theta_{123}} < \frac{r}{a} < C_1 \end{cases} \quad (6)$$

where C_2 is a constant determined by the geometry of the frames which is defined by $S = C_2 a^2$, S is the surface area of the polyhedron; α is the dihedral angle of the polyhedron; n is the number of edges of the polyhedral frames. The physical meaning of the dimensionless ratio $\frac{r}{a}$ is a coefficient related to the specific surface area of the solid frame, and its value is proportional to the ratio of the surface area of the polyhedron frame S_f to the surface area of the polyhedron S, that is $\frac{r}{a} \propto \frac{S_f}{S}$. The specific values of C_2, n, and boundary conditions for OFNs of different geometries are summarized in Text S2 (Supporting Information).

Taking the OFNs composed of truncated icosahedron frames to manipulate continuous water flow in air as an example (Figure 2F), we show how to use Equation (6) to guide the de-

sign of OFNs. For the case of $\theta_{123} = 0$, the theoretical boundary conditions for OFNs consisted of truncated icosahedral frames to form spontaneous capillary flows of water in air include

$$\begin{cases} a - 1.155r < 1.56 \text{ mm} \\ 0.145 < \frac{r}{a} < 0.866 \end{cases} \quad (7)$$

These boundary conditions are plotted in Figure 2F; the highlighted purple area includes the safe geometric parameters for forming spontaneous capillary flows in OFNs. To verify this conclusion, OFNs consisted of truncated icosahedron frames with different r and a are printed and tested, and the experimental results are marked in Figure 2F using distinct icons. The triangle represents successful creation of spontaneous capillary flow, and the cross indicates no spontaneous capillary flow (detailed in Figure S13, Supporting Information). It suggests that the experimental results are in good agreement with the theoretical predictions. In addition, using experiments, we also verified that the design principles of OFNs of other geometries also follow the boundary conditions of Equation (6).

To isolate the influence of contact angle θ_{123} on the design of OFNs, we compared the variation of the allowable minimum value of $\frac{r}{a}$ for OFNs of different geometries $[\frac{r}{a}]_{min}$ as the contact angle θ_{123} changes. The $[\frac{r}{a}]_{min}$ -θ_{123} curves indicate that for OFNs of different geometries, the $[\frac{r}{a}]_{min}$ always increases with the increase of θ_{123}, that is, as the wettability of the frame decreases, a larger specific surface area of the solid frame is required to provide capillarity to trigger spontaneous capillary flow. Under the same θ_{123}, the $[\frac{r}{a}]_{min}$ of OFNs of different geometries is ranked from small to large as follows: icosahedron, cube, dodecahedron, and truncated icosahedron (Text S2, Supporting Information), suggesting that, compared with other geometries, the specific surface area of the solid frame required to form spontaneous capillary flow in the icosahedral frames is the smallest under the same wettability.

For the connecting rods between the polyhedral frame units, both the theoretical analysis (detailed in Text S2, Supporting Information) and experiments show that at least two connecting rods are required to form spontaneous capillary flow in the OFNs, while one connecting rod cannot form spontaneous capillary flow, so the single-rod connection can act as a stop valve in the OFNs. Under reasonable pump speed ranges (capillary-dominated flow conditions), only when the single rod length is extremely short and the liquid reaches a supersaturated state, the continued fluid injection elevates internal pressure, transitioning the system to a pressure-driven regime that forces subsequent fluid into adjacent units, causing stop valve failure. To ensure reliable operation, the rod length must be designed with a minimum safety length to prevent unintended pressure-driven bypass. Taking the truncated icosahedral frames as an example, the critical safety threshold is 0.2 mm (Figure S14, Supporting Information).

Once the spontaneous capillary flow is formed in the OFNs, the velocity of the flow is mainly determined by the driving capillarity provided by the OFNs which can be flexibly adjusted by changing the surface wettability, geometric parameters, and spatial arrangement of the frames and connecting rods. Taking the OFNs composed of different geometries to manipulate continuous water flow in the air as an example, we examined how the dimensionless geometric parameter $\frac{r}{a}$ affects the average flow rates of the spontaneous capillary flows $\bar{v}$. As shown in Figure 2G, for polyhedral frames of different geometries, the $\bar{v}$ always increases with the increase of $\frac{r}{a}$, that is, a larger specific surface area of the frames provides a greater capillary driving force, thus resulting in a faster spontaneous capillary flow.

For the flow along the gravity direction, gravity and capillary force are both driving forces for spontaneous capillary flow, so continuous flow can be formed as long as Equation (6) is satisfied. For the flow against gravity, the capillary force provided by OFNs needs to overcome gravity, so there is a maximum capillary rise height H_{max}. From the perspective of energy, with the formation of the capillary flow against gravity, the surface energy of the system E_γ decreases and the gravitational potential energy E_g increases (Figure 2H). When the total energy of the system E does not change with liquid height h, the liquid reaches the maximum capillary rise height. That is, H_{max} occurs when

$$\frac{dE}{dh} = 0 \quad (8)$$

Based on the experimental results, the H_{max} always covers an integer number of polyhedral frame units in the OFNs. Based on Equation (8), the general expression for H_{max} of any OFNs is

$$H_{max} = \frac{\gamma_{lg}}{\rho g} * \frac{\left[A_{ls}\cos\theta - A_{lg}\right]_{unit}}{\left[V_l\right]_{unit}} + \frac{L_s}{2} \quad (9)$$

where γ_{lg} is the surface tension between liquid and gas; A_{lg}, A_{ls} are the created interfacial areas between the liquid and gas, and contact areas between the liquid and the solid frames, respectively; θ is the contact angle between the liquid and the solid frame; $[A_{ls}\cos\theta - A_{lg}]_{unit}$ is the value of $A_{ls}\cos\theta - A_{lg}$ of one frame unit; $[V_l]_{unit}$ is the volume of liquid in one frame unit; L_s is the length of connecting rod (the shorter rod), as well as the distance between two adjacent polyhedral frame units. The detailed derivation of Equation (9) is included in Text S3 (Supporting Information).

For OFNs of different geometries, substituting the specific geometric parameters of the frames, the general expression of H_{max} is obtained as follows,

$$H_{max} = \left[\frac{\gamma_{lg}}{\rho g}\frac{(\pi - 2\theta + \alpha)\left(a - \frac{r\sin\theta}{C_1}\right)rn\cos\theta - C_2\left(a - \frac{r\sin\theta}{C_1}\right)^2}{C_3\left(a - \frac{r\sin\theta}{C_1} + 2r\sin\theta + 2r\cos\theta\tan\frac{\pi-\alpha}{2}\right)^3 - \left(\frac{\pi-2\theta+\alpha}{2} + \sin\theta\cos\theta + \cos^2\theta\tan\frac{\pi-\alpha}{2}\right)\left(a - \frac{2r}{\tan\frac{\phi}{2}}\right)nr^2} + \frac{L_s}{2}\right] * \varphi \quad (10)$$

where C_3 is a constant determined by the geometry of the frames which is defined by $V = C_3\, a^3$, V is the volume of the polyhedron; φ is the correction factor reflects the deviation between theoretical analysis and experimental results, which may be caused by the 3D printing and experimental processes. Nondimensionalizing H_{max} with a yields

$$\frac{H_{max}}{a} = \left[\frac{\gamma_{lg}}{\rho g a^2} \frac{(\pi - 2\theta + \alpha)\left(1 - \frac{r}{a}\frac{\sin\theta}{C_1}\right)\frac{r}{a} n\cos\theta - C_2\left(1 - \frac{r}{a}\frac{\sin\theta}{C_1}\right)^2}{C_3\left(1 - \frac{r}{a}\frac{\sin\theta}{C_1} + 2\frac{r}{a}\sin\theta + 2\frac{r}{a}\cos\theta\tan\frac{\pi-\alpha}{2}\right)^3 - \left(\frac{\pi-2\theta+\alpha}{2} + \sin\theta\cos\theta + \cos^2\theta\tan\frac{\pi-\alpha}{2}\right)\left(1 - \frac{2r}{a\tan\frac{\phi}{2}}\right) n\left(\frac{r}{a}\right)^2} + \frac{L_s}{2a} \right] * \varphi \tag{11}$$

To verify the validity of Equation (11), we plotted the theoretically calculated and experimentally measured $\frac{H_{max}}{a} - \frac{r}{a}$ curves for OFNs of different geometries. In the experiment (Figure S15, Supporting Information), the contact angle of water on the solid surfaces of the OFNs is 0° and $L_s = 0.5$ mm, so θ and L_s are also set to these values in the theoretical calculations. As shown in Figure 2I, the $\frac{H_{max}}{a}$ always increases with the increase of $\frac{r}{a}$ for OFNs of different geometries, which is attributed to the fact that a larger specific surface area of the frame can provide greater capillary force, thereby supporting a larger capillary rise height. In addition, the experimental results are in good agreement with the theoretical calculations, supporting that H_{max} can be controlled by designing the frame's shape and size. Through appropriate wettability modification and geometric design, a variety of continuous flows have been successfully manipulated using OFNs of different geometries, including ethanol in air, glycerine in air, air in water, CCl_4 in water, and water in dimethyl silicone, which validates the wide applicability of OFNs to different fluidic systems (Figure 2J; Figure S16 and Movie S5, Supporting Information).

2.3. 3D Programmable Manipulation of Multiple Flows and Applications

OFNs provide a powerful fluidic platform capable of accurately and flexibly programming unary, binary, and multiple 3D continuous flows, which is critically required across diverse domains such as engineering manufacturing,[12] microfluidics,[21] biological detection,[22] chemical synthesis.[23,24] Utilizing selective metallization as an example, we illustrate the potential of OFNs in the fabrication of functional devices. The desired flow path of the fluid manipulated within the OFNs can be programmed by predesigning the distribution of single-rod and double-rod connections between the polyhedral frame units. The design principle dictates that double-rod connections are established between the frame units along the target path, while single-rod connections are set between frame units beyond the target path (**Figure 3A**). As depicted in Figure 3B, the activation liquid is introduced from a predetermined injection point to activate the frame units and connecting rods within the designated path in the OFNs, while other frame units remain inactive. Subsequently, an electroless plating solution is injected into the target path to metallize the frame units and connecting rods within that path, thereby creating the desired 3D conductive path within the OFN array structure.

The distinctive open structure of OFNs allows each polyhedral frame's free interfaces to function as an entry and exit for fluids, significantly facilitating the 3D programmable manipulation of multiple continuous flows. The desired 3D paths for multiple continuous flows can be achieved by designing the inlets for various fluids and the connecting rods between the frame units in the OFNs. For instance, 3D and 2D Y-shaped flow paths (Figure 3C,D) can be readily established by employing the connecting rod design principle illustrated in Figure 3A to regulate the mixing process of binary continuous flows (Movie S6, Supporting Information). The use of OFNs for controlling the mixing process not only provides a vivid visualization of the 3D mixing dynamics but also makes the production of mixtures with varying extents of mixing become accessible at any specified location, which is unattainable with conventional microfluidic systems. As demonstrated in Figure 3C, when equal volumes and flow rates of orange and blue-dyed aqueous solutions are injected for mixing, it is easy to obtain mixtures with different extents of mixing at various positions along the flow path at any given moment, with the resultant products easily extractable from the free interfaces. A more specific application is illustrated in Figure 3D, where intermittent injection and mixing of blue and orange-dyed ethanol solutions yield different colored mixtures at various positions within the OFNs at any moment. Consequently, the desired mixed color can be achieved by programming the injection timing and flow rates of the blue and orange solutions, facilitating precise color matching and artistic creation. To elucidate the liquid mixing dynamics in OFNs, numerical simulations of water–ethanol aqueous solution mixing are conducted (Figure S17 and Movie S7, Supporting Information). Molecular diffusion is identified as the dominant mechanism for mixing in OFNs under ultralow Reynolds number conditions (Re ≈ 1.4), and the mixing extent demonstrates a time-dependent progression wherein prolonged contact duration significantly expands the mixing zone. Taking the double-rod connection of icosahedral and truncated icosahedral frames as examples, the effect of $\frac{r}{a}$ on mixing efficiency are explored. With the increase of $\frac{r}{a}$, the mixing efficiency increases in both truncated icosahedral and icosahedral OFNs. Increased $\frac{r}{a}$, corresponding to a higher solid fraction within the microchannel, elevates the flow velocity per unit cross sectional area under a constant volumetric flow rate. This amplification in interfacial shear stress enhances fluid layer deformation and

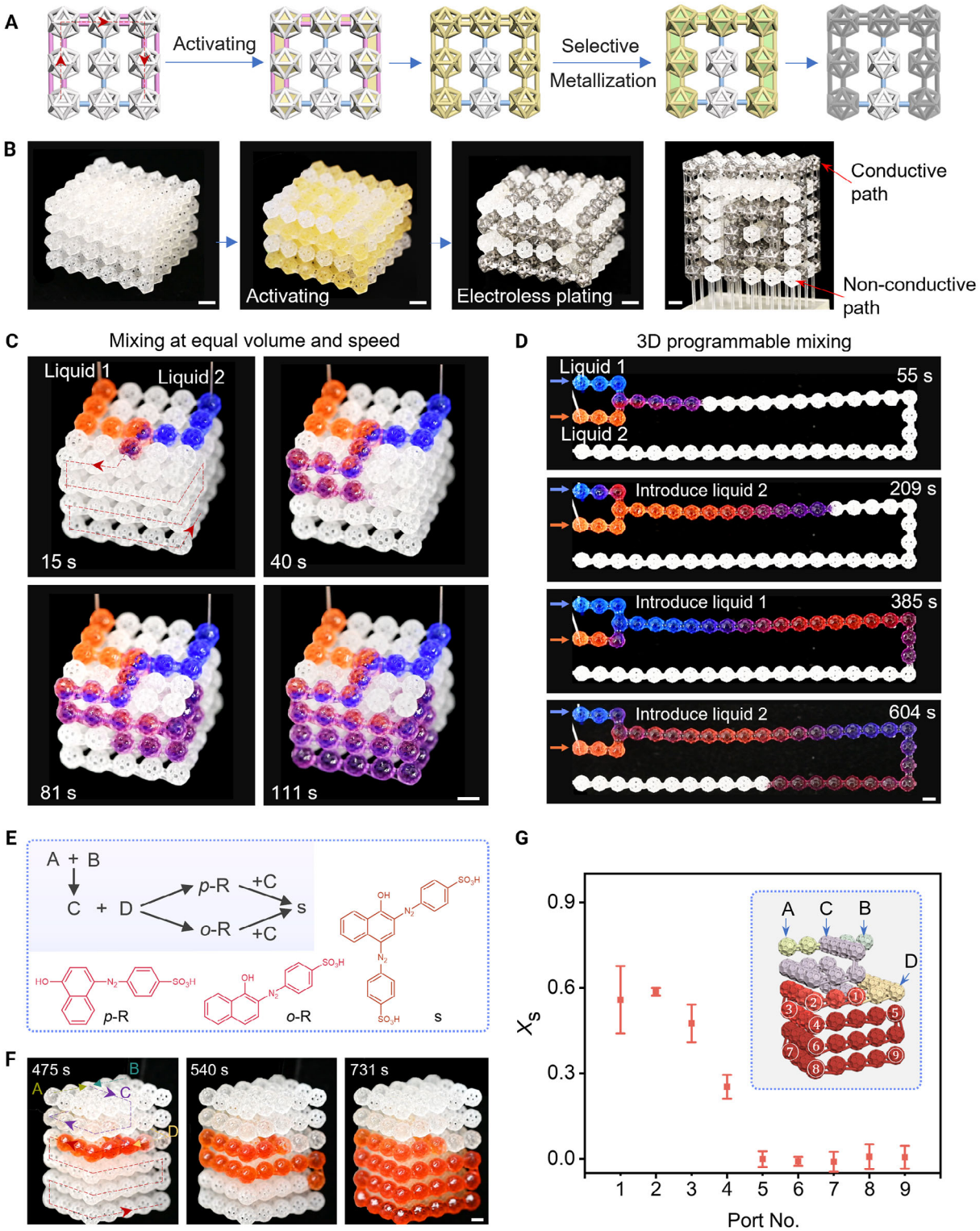

Figure 3. 3D programmable manipulation of multiple flows and applications. A) Schematic diagram of selective metallization process enabled by nickel electroless deposition. B) Selective metallization with the pre-programmed 3D OFNs. Scale bar, 5 mm. C,D) 3D spatiotemporal control of two continuous flow mixing processes by OFNs. Two continuous flows of dyed water are mixed at equal volumes and flow rates (C), and two continuous flows of dyed ethanol are mixed by intermittent alternating injection (D). Fluids have been dyed by different dyes to facilitate visualization. The details are provided in the Experimental Section. E) Multi-step reaction of diazo-coupling. F) 3D spatiotemporal control of multi-step reaction processes by OFNs. G) Dependence of the value X_s of the sampled liquids contained in the frames along the main path on the position of the frame units. In C, D, and F, the scale bars are 2 mm.

interdiffusion, thereby promoting mixing efficiency within the laminar flow regime. Besides, the splitting function of OFNs enables simultaneous multiplexed detection through spatially segregated microfluidic pathways (Figure S18, Supporting Information). Utilizing 3D fluidic architectures of OFNs enables spatially distributed multi-channel parallelism, which is expected to facilitate the development of high-throughput detection platforms for real-time disease monitoring.[25–27]

The unique capabilities of OFNs for manipulating multiple continuous flows are also promising for precise 3D spatiotemporal control of multi-step chemical reactions. Utilizing the diazo coupling reaction[28,29] as a case study, we quantitatively assessed the advantages of OFNs as multifunctional chemical reactors. By designing the inlet positions of different reactants and the arrangement of single-rod and double-rod connections between the frames, the expected 3D path of the chemical reaction is obtained. As shown in Figure 3F, reactants A and B are introduced by independent flow paths on either side of the OFNs array structure (yellow-green and green dashed lines), subsequently mixing and reacting in the confluence path (purple dashed line) to produce reactant C. This product is then mixed and reacted with reactant D, which is introduced via an independent path on the right side of the array (yellow dashed line), within the main path (red dashed line) to yield the final product (Figure S19 and Movie S8, Supporting Information). Specifically, reactants A and B are sulphanilic acid and sodium nitrite, respectively, resulting in the mixed product C, which is diazotized p-aminobenzenesulfonic acid, while reactant D is 1-naphthol. The reaction products formed from the mixing of C and D are contingent upon their respective ratios; when C is present in lesser amounts compared to D, the resulting products are isomeric monoazo dyes (*p*-R and *o*-R), whereas a higher concentration of C relative to D yields bisazo dye (s). As the reaction progresses, the mixture of A and B, exhibiting varying extents of reaction, combines with D in the main path and continues to flow forward, resulting in a red coloration indicative of azo dye formation. Consequently, at any given moment, the composition of the reactants within each frame unit along the main path differs, leading to variations in product composition. Five minutes after the mixture occupied the main path, equal volumes of liquid were extracted from frame units at various locations to analyze their product compositions. The segregation index X_s is employed to quantitatively characterize the concentration of bisazo dye (s) in the sampled liquids. The mathematic expression of X_S is

$$X_s = \frac{2C_s}{C_{p-R} + C_{o-R} + 2C_s} \tag{12}$$

where C_{p-R}, C_{o-R}, and C_s are the concentrations of the products *p*-R, *o*-R and s, respectively. The larger the X_s value, the higher the content of the bisazo dye.[30] The experimental findings indicate that along the main path, specifically from port 1 to port 9 as illustrated in Figure 3G, the concentration of bisazo dye exhibits a gradual decline from ≈0.6 to 0. This trend suggests a diminishing presence of bisazo dye, which can be attributed to the increasing reaction extent between reactants A and B, leading to a corresponding rise in the concentration of reactant C. Consequently, as the injection of the A and B mixture progresses from the most recent to the earliest time points along the main path, the concentration of reactant C decreases sequentially, resulting in a lower detection of bisazo dye. Thus, the utilization of OFNs as chemical reactors allows for precise temporal and spatial control over the reaction process within each frame unit. This capability facilitates the collection of reaction products with varying compositions at specific moments, thereby significantly enhancing the efficiency of chemical synthesis for batch production and the harvesting of differentiated products.[31,32]

2.4. Enhancement of Interfacial Mass and Heat Transfer with the OFNs

Fluid interfaces are ubiquitous in nature and industrial production, and the precise control of interfacial processes is essential for various applications. While open fluid networks (OFNs) are designed to manipulate continuous flows, they also facilitate the structuring of fluids and the formation of stable 3D fluid interfaces, thereby serving as a versatile platform for the engineering of interfacial processes. To further increase the free interfacial area of OFNs to enhance interfacial processes, the connecting rods between frame units are removed, allowing for the direct connection of polyhedral frame units to create an open channel structure (Figure S20, Supporting Information). The potential of OFNs in enhancing interfacial processes is explored by examining the interfacial mass transfer and heat transfer processes. Through the interfacial gelation, a semipermeable hydrogel membrane can be generated on the surface of OFNs, enabling controlled drug release. As depicted in **Figure 4A,B**, solution A (calcium chloride) is introduced into the OFNs, which are subsequently immersed in solution B (sodium alginate) to facilitate interfacial gelation, resulting in a free-standing 3D gel membrane. Effective controlled drug release is only observed in membrane-covered OFNs, as opposed to those without a membrane, thereby confirming the integrity of the membrane and the efficacy of the interfacial gelation method (Figure 4C; Figure S21, Supporting Information). Doxorubicin hydrochloride, a chemotherapeutic agent utilized in the treatment of various cancers, was selected as the model drug. The aqueous solution containing doxorubicin hydrochloride was injected into the membrane-covered OFNs, and the drug release process was evaluated in distilled water at varying pH levels. The experimental results demonstrate that the release rate and equilibrium concentration of the drug are greater in water with a pH of 5 compared to water with a pH of 7 (Figure 4D). This phenomenon can be attributed to the reduction in membrane thickness and the increase in porosity and pore size, which occur as the hydrogel membranes shrink and undergo partial hydrolysis due to proton exchange in acidic solutions. SEM imaging of the membranes corroborated this conclusion, revealing a significant increase in both porosity and pore size of the hydrogel membranes in water with a pH of 5 (Figure 4D).

In contrast to conventional closed piping systems, OFNs offer precise control over continuous flow while maintaining free interfaces for fluid interaction with the surrounding environment. The application of OFNs in heat exchangers overcomes the limitations imposed by pipe walls on heat exchange efficiency, thereby facilitating the development of a novel type of efficient wall-less heat exchanger. As illustrated in Figure 4E, OFNs were

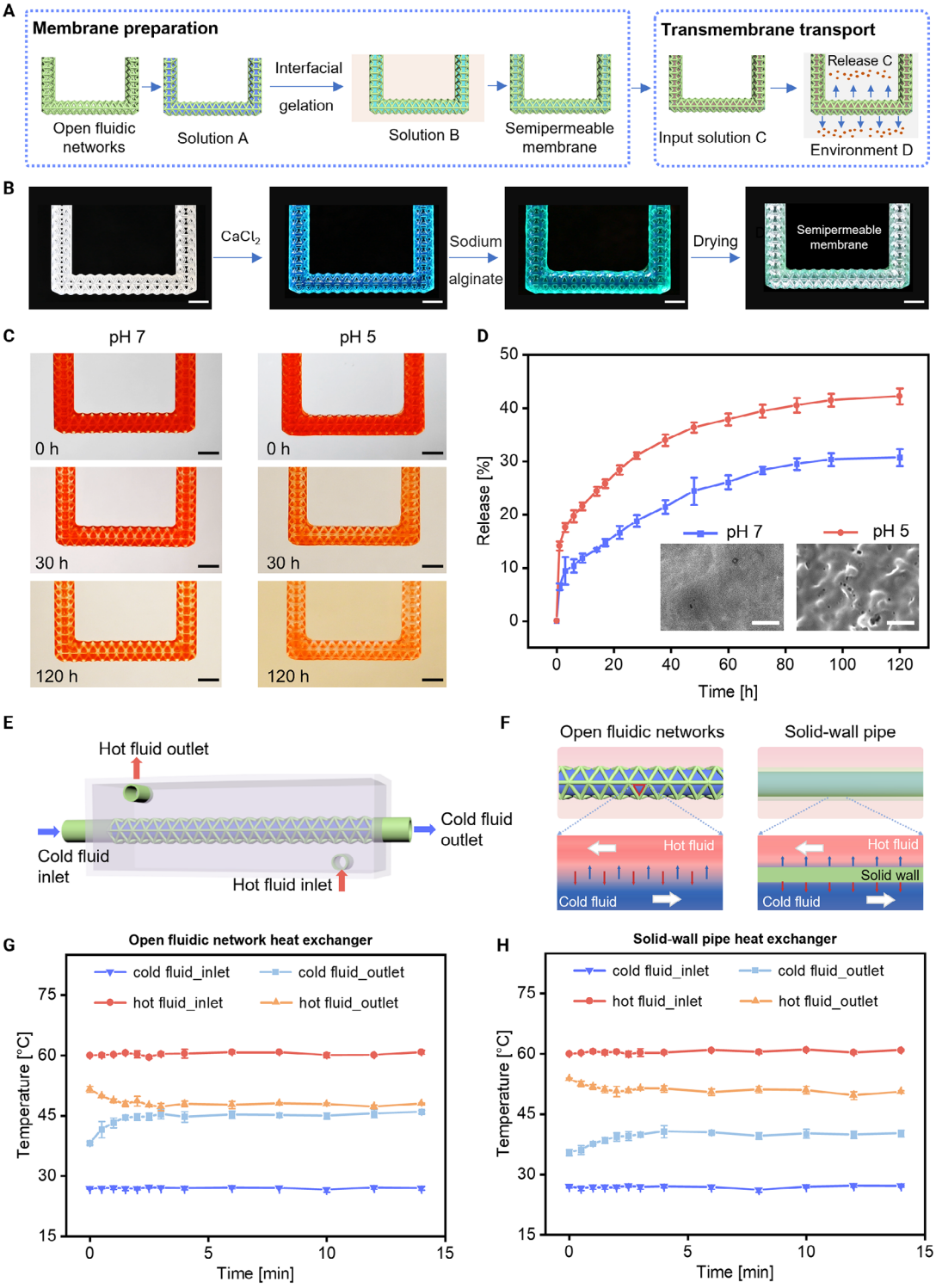

Figure 4. Enhancement of interfacial mass and heat transfer with the OFNs. A) Schematic diagram of membrane preparation of the OFNs via interfacial gelation and interfacial mass transfer. B) Preparation of semipermeable membrane on the OFNs through the gelation reaction of $CaCl_2$ and sodium alginate. $CaCl_2$ and sodium alginate solutions are dyed by blue and yellow dyes to facilitate visualization, respectively. The details are provided in the Experimental Section. C) The controlled release of doxorubicin hydrochloride captured in the OFNs in water at different pH. D) Corresponding release profiles of doxorubicin hydrochloride in water at different pH. The insets show the SEM images of the membranes on the OFNs after drug release experiments. Scale bar, 1 µm. E) Schematic diagram of the OFNs-based counter-flow double-pipe heat exchanger. F) Differences between heat exchange processes in OFNs-based heat exchanger and traditional heat exchanger. G,H) Temperature-time curves of the inlet and outlet for both the cold and hot fluids in the OFNs-based heat exchanger (G) and traditional heat exchanger (H). In B and C, the scale bars are 5 mm.

utilized as an inner pipe in the classic counter-flow double-pipe heat exchanger for the transport of cold fluid (water at an inlet temperature of 27 °C) within an immiscible hot fluid (paraffin at an inlet temperature of 61 °C). OFNs-based heat exchanger demonstrates excellent liquid–liquid interfacial stability during fluid flow through appropriate structural design (Figure S22, Supporting Information). For comparative analysis, a conventional heat exchanger was constructed, which differed from the OFNs-based system by employing a closed pipe of equivalent diameter, fabricated from the same material, to serve as the inner pipe for cold fluid transport (Figure 4F). The temperature profiles of the inlet and outlet for both the cold and hot fluids in the two heat exchangers were monitored over time (Figure 4G,H). The findings indicated that OFNs facilitate ultra-efficient heat exchange, with the outlet temperature of the cold fluid reaching 46 °C and the outlet temperature of the hot fluid at 48 °C, demonstrating a close thermal proximity. A quantitative comparison of the heat transfer performance was conducted by calculating the overall heat transfer coefficient (U) and effectiveness (ϵ) for both heat exchangers (Text S4, Supporting Information). The overall heat transfer coefficient and effectiveness of the OFNs-based heat exchanger are 1.7 times and 1.23 times those of the solid-wall pipe heat exchanger, respectively. Besides, stainless steel and fluorinated polymers (e.g. polytetrafluoroethylene, PTFE) are commonly employed as microfluidic tubing materials. The respective U and ϵ values of solid-wall heat exchangers based on these materials can be theoretically estimated using established formulas (Text S4, Supporting Information). The results show that for the OFNs-based heat exchanger, the U and ϵ values are 1.15 times and 1.05 times those of stainless steel-based solid-wall pipe heat exchanger, and 1.26 times and 1.10 times those of PTFE-based solid-wall heat exchanger, respectively. Therefore, as a versatile platform for continuous flow control, OFN can be widely used in miscible and immiscible fluid systems, greatly facilitating various interfacial processes.

3. Conclusion

In conclusion, we have demonstrated that the OFNs can facilitate precise, programmable, and 3D spatiotemporal manipulation of continuous flow through the utilization of capillary forces to induce spontaneous capillary flow. The polyhedral frame units of OFNs serve as fluid chambers capable of storing and transporting a diverse array of fluids, while the connecting rods between these frame units function as effective valves allowing for flexible and convenient adjustments to the direction, speed, and path of the continuous flow. The free interfaces maintained by the frames act as portals for interaction between the fluid and its surrounding environment, ensuring unrestricted entry and exit of the fluid at any designated location. The straightforward yet effective architecture of OFNs confers multiple functionalities, establishing it as a versatile fluidic tool that can be broadly applied across various fluidic systems. The design of OFNs does not necessitate complex equipment or cumbersome manufacturing; rather, its adaptable structural design can be tailored to suit different application scenarios and requirements. Simply by modifying the base materials and structural configurations of OFNs and integrating them with various fluid systems, their applicability can be extended to numerous domains, including engineering, biology, chemistry, medicine, materials science, and energy. For instance, OFNs constructed from biocompatible materials may be employed for controlled drug delivery, tissue engineering, and regenerative medicine in vivo.[33,34] The programmable manipulation and structuring capabilities of OFNs for a range of continuous fluids enable 3D spatiotemporal control over biological and chemical processes, as well as the enhancement of interfacial phenomena. Furthermore, the 3D membrane structures developed on OFNs can be utilized to investigate biological transmembrane behaviors, such as mimicking alveolar-capillary barriers,[35] gastrointestinal absorption,[36] and glomerular filtration.[37] The advent of such a powerful fluidic platform is poised to establish new benchmarks for controllability, versatility, and performance in the precise manipulation of continuous flows, significantly advancing research and applications that involve fluid interfacial processes and fostering scientific and technological innovation across multiple fields, including engineering, microfluidics, interfacial chemistry, and biomedicine.

4. Experimental Section

Fabrication of the OFNs: The OFNs composed of polyhedral frames and connecting rods were fabricated by 3D printing using a commercial Low Force Stereolithography printer Formlabs Form 3+. All parts were printed with the commercial resin—Clear Resin (FLGPCL04) in a layer-by-layer manner (25-µm layers). Isopropanol was used for the post-clean process for 15 min and all parts were further cured for 15 min at 60 °C under blue light (10 mW cm^{-2}, 420 nm).

Surface Modification: To obtain the superhydrophilic wettability, the process involves three steps: a) surface cleaning with plasma treatment; b) surface modification with superhydrophobic spray; c) plasma activation for hydrophilicity enhancement. The details were as follows: the solid frames were first exposed to O_2 plasma for 15 min with a plasma cleaner (Harrick Plasma Cleaner) at radio-frequency power of 45 W. After plasma treatment, all parts were immersed in the commercial water repellent (Glaco Mirror Coat Zero, Soft 99 Ltd, Japan) at room temperature for 5 min to introduce silica-based coatings. After drying naturally in the air, all parts were exposed to O_2 plasma for 15 min to modify the surface wettability from hydrophobicity to hydrophilicity.[38]

Contact Angle Measurement: A goniometer (SindatekOptical Video-based Contact Angle Meter-100SB) is used to measure the contact angle of different liquids with printed parts before and after surface modification. Before modification, contact angles were 82.7°, 71.1°, 60.1°, 29.7°, 18.1°, 0°, and 15.6°for water, glycerin, ethylene glycol, ethanol, paraffin, dimethyl silicone, and carbon tetrachloride (CCl_4), respectively. After modification, contact angles were 0°, 18.7°, 5.4°, 0°, 4.3°, 0°, and 0° for the above liquids, respectively.

Manipulation of Various Continuous Fluids Using OFNs: A simple reservoir provides liquid for OFNs to form spontaneous capillary flow. Once polyhedral frames contact with the liquid, capillary forces drive the liquid to spontaneously enter the channel and flow. Liquid flows could also be constructed by syringe needles connected to a microsyringe pump (LSP01-1A) at an injection rate of 50 µL min^{-1}. To visualize, different edible dyes including blue, yellow, orange, and red edible dyes were mixed with water, respectively (Figures 1, 2H, and 3C; Figures S10, S12–S15, S20, S22, Supporting Information). In Figure 2J, ethanol, glycerin, and water were mixed with pink, yellow, and blue edible dyes, respectively. CCl_4 was mixed with green oil-soluble dye. In Figure 3D, ethanol is mixed with blue and orange edible dyes, respectively. In Figure S16 (Supporting Information), ethylene glycol, glycerin, and water were mixed with green, red, and blue edible dyes, respectively. Paraffin was mixed with orange oil-soluble dye. All dyes were mixed with corresponding liquids at the concentration of 0.1%–0.5% wt.

Selective Metallization: The process of nickel plating by chemical reduction on printed 3D structures primarily consists of two steps: activation and nickel plating. Palladium acetate was dissolved in acetone to

prepare the activation solution (0.3 g L^{-1}). The chemical plating solution was a mixture of two aqueous solutions: A and B (A:B = 4:1, *v/v*). Solution A contains nickel sulfate (5 g L^{-1}), sodium citrate (20 g L^{-1}), and lactic acid (10 g L^{-1}); Solution B was dimethylamine borane aqueous solution (DMAB, 0.01 g L^{-1}). Before using, the pH of Solution A was adjusted to 8–10. The activation solution was first filled into the pre-programmed paths. After waiting for 30 min, the plating solution was injected into the pre-programmed paths to complete the metallization process. Deionized water rinsing was performed between the steps.

3D Spatiotemporal Control of Fluid Mixing Processes with OFNs: Liquid mixing was performed by two different injection modes. In Figure 3C, water streams colored by blue and orange edible dyes were used to demonstrate. Two liquids were injected into the OFNs at a constant flow rate (25 µL min^{-1}). In Figure 3D, ethanol streams colored by blue and orange edible dyes are used to demonstrate. After mixing, two liquids were injected following the procedure: introduce liquid 1 and 2 simultaneously (50 s)→introduce liquid 2 (130 s)→introduce liquid 1 and 2 simultaneously (50 s)→introduce liquid 1 (130 s)→introduce liquid 1 and 2 simultaneously (50 s) →introduce liquid 2 (120 s) →introduce liquid 1 and 2 simultaneously (50 s). The flow rate was 25 µL min^{-1}.

Dual-Modal Detection of Hydroxide Ions (OH^-): Iron (III) chloride aqueous solution ($FeCl_3$, 0.28 mol L^{-1}) and phenolphthalein aqueous solution (0.006 mol L^{-1}) were pre-incorporated into the OFNs. Subsequently, NaOH (0.63 mol L^{-1}) aqueous solution were pipetted into the OFNs until color changes occur, triggered by the interaction of NaOH with phenolphthalein (turning red) and iron(III) chloride (forming a brown $Fe(OH)_3$ precipitate).

Diazo-Coupling Reactions in the OFNs: Sulphanilic acid was dissolved in hydrochloric acid (0.5 mol L^{-1}) to obtain solution A (5.8 mmol L^{-1}). Sodium nitrite was dissolved in deionized water to obtain solution B (6.96 mmol L^{-1}). The buffer solution was prepared using Na_2CO_3 and $NaHCO_3$ (pH = 10.1, ionic strength (*I*) is 0.440 mol L^{-1}). 1-naphthol was first dissolved in ethanol and then mixed with the buffer solution at a ratio of 20% (*v/v*) to form solution D, ensuring a final 1-naphthol concentration of 6.96 mmol L^{-1}. Solutions A and B are simultaneously injected into the OFNs at the flow rate of 15 µL min^{-1}. After mixing, they react to form diazotized p-aminobenzenesulfonic acid (solution C). This product was then mixed and reacted with reactant D, which was introduced at a flow rate of 60 µL min^{-1}, within the main path to yield the final products. After the mixture occupies the main path, wait 5 min to collect the products. The samples were diluted to standard conditions (*I* = 0.0440 mol L^{-1}) and analyzed in the spectrophotometer. The absorption of each sample in the wavelength range of 300–700 nm is recorded by the Varian Cary 4000 UV-Visible Spectrophotometer. The concentrations of different dyes (*p*-R, *o*-R, and s) could be determined by performing multilinear regression analysis on the absorbance at different wavelengths according to Lambert–Beer's law and the following formula:

$$E\ (\lambda) = \varepsilon_{p-R}\, bc_{p-R} + \varepsilon_{o-R} bc_{o-R} + \varepsilon_s bc_s \tag{13}$$

where $E(\lambda)$ is absorbance; ϵ is the molar extinction coefficient of the corresponding product (unit, m^2 mol^{-1}); *b* is the width of the cuvette (unit, m); *c* is the molar concentration of the corresponding product (unit, mol m^{-3}). The following shows molar extinction coefficients of the three products ($T = 25$ °C, $I = 0.0440$ mol L^{-1}, pH = 10): at 510 nm, the values of ϵ are 3170 (*p*-R), 2380 (*o*-R) and 1880 (s) m^2 mol^{-1}; at 520 nm, the values of ϵ are 3160 (*p*-R), 2320 (*o*-R) and 1940 (s) m^2 mol^{-1}; at 560 nm, the values of ϵ are 1570 (*p*-R),1020 (*o*-R) and 2320 (s) m^2 mol^{-1}.[39]

Membrane Preparation with the OFNs and Controlled Drug Release: The concentrations of $CaCl_2$ and sodium alginate solutions used in Figure 4B–D for membrane preparation were 2 wt.% and 1 wt.%, respectively. To visualize, $CaCl_2$ and sodium alginate were stained separately by blue and yellow edible dyes at the concentration of 0.1%–0.5% wt. The following was the preparation process of the membrane: the OFNs were first filled with $CaCl_2$ solution, then immersed in sodium alginate solution for 2 min, and then washed with distilled water. Later, they were immersed in $CaCl_2$ solution for 1 min to stabilize the membranes and washed with distilled water again. After natural drying, the green semipermeable membrane in Figure 4B was formed. For drug transmembrane release, doxorubicin hydrochloride was dissolved in distilled water (1 mg mL^{-1}) and introduced into membrane-covered OFNs. The OFNs loaded with doxorubicin hydrochloride were placed into distilled water with pH of 1 and 5 (130 mL). The release profiles of doxorubicin hydrochloride shown in Figure 4D were carried out by testing solution absorbance at 250-nm wavelength by UV-visible spectrometer. After being treated with water of different pH for 120 h, the OFNs with membranes were subjected to freeze-drying using the Labfreez FD-12R-80C Freeze Dryer. The microstructures of the dried membranes were observed by Scanning Electron Microscope (SEM, Tescan VEGA3).

Efficient OFNs-Based Heat Exchanger: All parts of heat exchangers were fabricated by 3D printing according to the dimensions provided in Text S4 (Supporting Information). The components are assembled as shown in Figure 4E, with sealing tapes applied to ensure leak-proof integrity. Water and liquid paraffin were used as the cold fluid and hot fluid, respectively. The inlet temperature was 27 °C for water and 61 °C for paraffin. Paraffin was preheated using an adjustable digital hot plate (Barnstead/Thermolyne Cimarec, Thermo Scientific), and maintained at the stable temperature via a digitally controlled heating sleeve on the syringe. Water was maintained at ambient temperature. The temperature variation was ±1 °C. Temperature measurements were taken using thermocouples (Omega Type K). Cold fluid and hot fluid were injected at volumetric flow rates of 1 and 3 mL min^{-1}, respectively. Before the experiment, water and paraffin were injected to check for leaks. The time starts when both the cold and hot fluid streams had filled their assigned flow channels within the heat exchanger. At scheduled time intervals, data points were collected.

Numerical Simulations: The finite element modeling of the fluid mixing processes was simulated using COMSOL Multiphysics 6.2. A two-phase flow module with Level Set and laminar flow interfaces was implemented, where water and an ethanol aqueous solution (17.12 mol L^{-1}) served as working fluids. The frame structure was defined with a fluid-solid contact angle of 0°. Both fluids were injected into the channel at a flow rate of 25 µL min^{-1}, with a diffusion coefficient of 1.20×10^{-9} m^2 s^{-1}. The transport of diluted species was used to resolve species concentration fields and hydrodynamic interactions. Mixing efficiency, e_{mixing}, at the outlet cross section of the microchannel was evaluated by the following parameter:

$$e_{mixing} = \left(1 - \frac{\iint_{cross\ section} |C - C_{Ideal}|\, dA}{\iint_{cross\ section} |C_0 - C_{Ideal}|\, dA}\right) \times 100\% \tag{14}$$

where, *A* is the outlet cross section area (m^2), *C* is outlet concentration (mol m^{-3}), C_{Ideal} is the ideal (complete) mixing concentration (mol m^{-3}) and C_0 is the concentration at the inlet for completely unmixed sample (mol m^{-3}).[40]

Supporting Information

Supporting Information is available from the Wiley Online Library or from the author.

Acknowledgements

L.W. acknowledges the financial support from the Research Grants Council of Hong Kong (GRF 17213823, 17205421, and 17204420) and the Hong Kong Polytechnic University (SHS Chair Professor: P0045687). Y.Z. acknowledges the financial support from the Hong Kong Polytechnic University (SHS Research Assistant Professor: P0047732). S.W. acknowledges Mr. Kin Wa Lui from the University Research Facility in 3D Printing (U3DP) at The Hong Kong Polytechnic University for his help in printing the molds.

Conflict of Interest

The authors declare no conflict of interest.

Author Contributions

S.W. and Y.Z. contributed equally to this work. Y.Z., S.W., and L.W. conceived and designed this work. Y.Z. and L.W. supervised the research. S.W. performed the experiments. S.S. helped with the SEM characterization. J.Y. conducted the numerical simulations of fluid mixing dynamics and contributed to the manuscript revision. S.W., Y.Z., and L.W. developed the theoretical model. S.W. and Y.Z. analyzed the data. S.W., Y.Z., and L.W. wrote and revised the manuscript.

Data Availability Statement

The data that support the findings of this study are available from the corresponding author upon reasonable request.

Keywords

3D open fluidic networks, capillary, connected polyhedral frames, continuous flow manipulation, multifunctional, programmable

Received: February 25, 2025
Revised: April 25, 2025
Published online: May 5, 2025

[1] K. Ronaldson-Bouchard, D. Teles, K. Yeager, D. N. Tavakol, Y. Zhao, A. Chramiec, S. Tagore, M. Summers, S. Stylianos, M. Tamargo, B. M. Lee, S. P. Halligan, E. H. Abaci, Z. Guo, J. Jacków, A. Pappalardo, J. Shih, R. K. Soni, S. Sonar, C. German, A. M. Christiano, A. Califano, K. K. Hirschi, C. S. Chen, A. Przekwas, G. Vunjak-Novakovic, *Nat. Biomed. Eng.* **2022**, *6*, 351.
[2] S. Maharjan, B. Cecen, Y. S. Zhang, *Small Methods* **2020**, *4*, 2000235.
[3] A. Guan, P. Hamilton, Y. Wang, M. Gorbet, Z. Li, K. S. Phillips, M. D. Chips, *Nat. Biomed. Eng.* **2017**, *1*, 0045.
[4] Z. Yi, X. Ma, Q. Tong, L. Ma, Y. Tan, D. Liu, C. Tan, J. Chen, X. Li, *Adv. Mater.* **2025**, *37*, 2417534.
[5] D. Perera, J. W. Tucker, S. Brahmbhatt, C. J. Helal, A. Chong, W. Farrell, P. Richardson, N. W. Sach, *Science* **2018**, *359*, 429.
[6] X. Fu, J. B. Pedersen, Y. Zhou, M. Saccoccio, S. Li, R. Sažinas, K. Li, S. Z. Andersen, A. Xu, N. H. Deissler, J. B. V. Mygind, C. Wei, J. Kibsgaard, P. C. K. Vesborg, J. K. Nørskov, I. Chorkendorff, *Science* **2023**, *379*, 707.
[7] X. Zheng, H. Lee, T. H. Weisgraber, M. Shusteff, J. DeOtte, E. B. Duoss, J. D. Kuntz, M. M. Biener, Q. Ge, J. A. Jackson, S. O. Kucheyev, N. X. Fang, C. M. Spadaccini, *Science* **2014**, *344*, 1373.
[8] F. Jiang, L. Zhan, J. P. Lee, P. S. Lee, *Adv. Mater.* **2024**, *36*, 2308197.
[9] B. Zhang, W. Xu, L. Peng, Y. Li, W. Zhang, Z. Wang, *Nat. Rev. Electr. Eng.* **2024**, *1*, 218.
[10] G. M. Whitesides, *Nature* **2006**, *442*, 368.
[11] H. R. Sahoo, J. G. Kralj, K. F. Jensen, *Angew. Chem., Int. Ed.* **2007**, *46*, 5704.
[12] N. A. Dudukovic, E. J. Fong, H. B. Gemeda, J. R. DeOtte, M. R. Cerón, B. D. Moran, J. T. Davis, S. E. Baker, E. B. Duoss, *Nature* **2021**, *595*, 58.
[13] F. Paratore, V. Bacheva, M. Bercovici, G. V. Kaigala, R. Microfluidics, *Nat. Rev. Chem.* **2022**, *6*, 70.
[14] Y. Zhang, Z. Huang, Z. Cai, Y. Ye, Z. Li, F. Qin, J. Xiao, D. Zhang, Q. Guo, Y. Song, J. Yang, *Sci. Adv.* **2021**, *7*, abi7498.
[15] A. J. deMello, *Nature* **2006**, *442*, 394.
[16] P. Zhang, Y. Liu, G. Feng, C. Li, J. Zhou, C. Du, Y. Bai, S. Hu, T. Huang, G. Wang, P. Quan, J. Hirvonen, J. Fan, H. A. Santos, D. Liu, *Adv. Mater.* **2023**, *35*, 2211254.
[17] Y. Wang, R. Jin, B. Shen, N. Li, H. Zhou, W. Wang, Y. Zhao, M. Huang, P. Fang, S. Wang, P. Mary, R. Wang, P. Ma, R. Li, Y. Tian, Y. Cao, F. Li, L. Schweizer, H. Zhang, *Sci. Adv.* **2021**, *7*, abe3839.
[18] S. Sun, J. Miao, R. Tan, T. Zhang, G. Li, Y. Shen, *Adv. Funct. Mater.* **2023**, *33*, 2209769.
[19] S. Sun, Y. Zhang, S. Wu, L. Wang, *Adv. Mater.* **2024**, *36*, 2407034.
[20] Y. Zhang, Z. Huang, F. Qin, H. Wang, K. Cui, K. Guo, Z. Cai, X. Cai, J. Xiao, J. Carmeliet, J. Wei, Y. Song, J. Yang, L. Wang, *Nat. Chem. Eng.* **2024**, *1*, 472.
[21] H. Luan, Q. Zhang, T.-L. Liu, X. Wang, S. Zhao, H. Wang, S. Yao, Y. Xue, J. W. Kwak, W. Bai, Y. Xu, M. Han, K. Li, Z. Li, X. Ni, J. Ye, D. Choi, Q. Yang, J.-H. Kim, S. Li, S. Chen, C. Wu, D. Lu, J.-K. Chang, Z. Xie, Y. Huang, J. A. Rogers, *Sci. Adv.* **2021**, *7*, abj3686.
[22] C. Lou, H. Yang, Y. Hou, H. Huang, J. Qiu, C. Wang, Y. Sang, H. Liu, L. Han, *Adv. Mater.* **2024**, *36*, 2307051.
[23] P. Gruner, B. Riechers, B. Semin, J. Lim, A. Johnston, K. Short, J.-C. Baret, *Nat. Commun.* **2016**, *7*, 10392.
[24] J. Britton, T. F. Jamison, *Nat. Protoc.* **2017**, *12*, 2423.
[25] X. Han, R. Jin, Y. Sun, K. Han, P. Che, X. Wang, P. Guo, S. Tan, X. Sun, H. Dai, Z. Dong, L. Heng, L. Jiang, *Adv. Mater.* **2024**, *36*, 2311729.
[26] X. Han, S. Tan, R. Jin, L. Jiang, L. Heng, *J. Am. Chem. Soc.* **2023**, *145*, 6420.
[27] X. Han, S. Tan, Q. Wang, X. Zuo, L. Heng, L. Jiang, *Adv. Mater.* **2024**, *36*, 2402779.
[28] J. R. Bourne, C. Hilber, G. Tovstiga, *Chem. Eng. Commun.* **1985**, *37*, 293.
[29] J. R. Bourne, O. M. Kut, J. Lenzner, H. Maire, *Ind. Eng. Chem. Res.* **1990**, *29*, 1761.
[30] H. Zhang, T. Kopfmüller, R. Achermann, J. Zhang, A. Teixeira, Y. Shen, K. F. Jensen, *AIChE J.* **2020**, *66*, 16873.
[31] A. Adamo, R. L. Beingessner, M. Behnam, J. Chen, T. F. Jamison, K. F. Jensen, J.-C. M. Monbaliu, A. S. Myerson, E. M. Revalor, D. R. Snead, T. Stelzer, N. Weeranoppanant, S. Y. Wong, P. Zhang, *Science* **2016**, *352*, 61.
[32] M. M. I. Rizk, G.-L. Davies, *Matter* **2024**, *7*, 2732.
[33] C. Yu, J. Schimelman, P. Wang, K. L. Miller, X. Ma, S. You, J. Guan, B. Sun, W. Zhu, S. Chen, *Chem. Rev.* **2020**, *120*, 10695.
[34] L. Moroni, J. A. Burdick, C. Highley, S. J. Lee, Y. Morimoto, S. Takeuchi, J. J. Yoo, *Nat. Rev. Mater.* **2018**, *3*, 21.
[35] B. Grigoryan, S. J. Paulsen, D. C. Corbett, D. W. Sazer, C. L. Fortin, A. J. Zaita, P. T. Greenfield, N. J. Calafat, J. P. Gounley, A. H. Ta, F. Johansson, A. Randles, J. E. Rosenkrantz, J. D. Louis-Rosenberg, P. A. Galie, K. R. Stevens, J. S. Miller, M. Networks, F. I. T. B. Hydrogels, *Science* **2019**, *364*, 458.
[36] W. A. Banks, *Nat. Rev. Drug Discovery* **2016**, *15*, 275.
[37] A. Petrosyan, P. Cravedi, V. Villani, A. Angeletti, J. Manrique, A. Renieri, R. E. De Filippo, L. Perin, S. D. Sacco, *Nat. Commun.* **2019**, *10*, 3656.
[38] B. Xu, Y. Ding, *Adv. Mater. Interfaces* **2022**, *9*, 2200934.
[39] K. S. Wenger, E. H. Dunlop, I. D. MacGilp, *AIChE J.* **1992**, *38*, 1105.
[40] R. Kamali, S. A. Shekoohi, A. Binesh, *Nano-Micro Lett.* **2014**, *6*, 30.